Intel RealSense SR305, D415 and L515: Experimental Evaluation and Comparison of Depth Estimation

Francisco Lourenço[a] and Helder Araujo[b]

Institute of Systems and Robotics, Department of Elec. and Comp. Eng.,University of Coimbra, Coimbra, Portugal

Abstract: In the last few years, Intel has launched several low-cost RGB-D cameras. Three of these cameras are the SR305, the L415, and the L515. These three cameras are based on different operating principles. The SR305 is based on structured light projection, the D415 is based on stereo based also using the projection of random dots, and the L515 is based on LIDAR. In addition, they all provide RGB images. In this paper, we perform an experimental analysis and comparison of the depth estimation by the three cameras.

1 INTRODUCTION

Consumer-level RGB-D cameras are affordable, small, and portable. These are some of the main features that make these types of sensors very suitable tools for research and industrial applications, ranging from practical applications such as 3D reconstruction, 6D pose estimation, augmented reality, and many more (Zollhöfer et al., 2018). For many applications, it is essential to know how accurate and precise an RGB-D camera is, to understand which sensor best suits the specific application (Cao et al., 2018). This paper aims to compare three models of RGB-D cameras from Intel, which can be useful for many users and applications.

The sensors are the RealSense SR305, D415, and L515. Each sensor uses different methods to calculate depth. The SR305 uses coded light, where a known pattern is projected into the scene and, by evaluating how this pattern deforms, depth information is computed. The D415 uses stereo vision technology, capturing the scene with two imagers and, by computing the disparity on the two images, depth can be retrieved. Finally, the L515 that measures time-of-flight, i.e., this sensor calculates depth by measuring the delay between light emission and light reception.

Several different approaches can be used to evaluate depth sensors (P.Rosin et al., 2019),(Fossati et al., 2013). In this case, we focused on accuracy and repeatability. For this purpose, the cameras were eval-

uated using depth images of 3D planes at several distances, but whose ground truth position and orientation were not used as we don't know them. Accuracy was measured in terms of point-to-plane distance, and precision was measured as the repeatability of 3D model reconstruction, i.e., the standard deviation of the parameters of the estimated 3D model (in this case, a 3D plane). We also calculated the average number of depth points per image where the cameras failed to calculate depth (and their standard deviation), and the number of outliers per image (points for which the depth was outside an interval). Moreover, we employ directional statistics (Kanti V. Mardia, 1999) on the planes' normal vectors to better illustrate how these models variate.

2 RELATED WORK

Depth cameras and RGB-D cameras have been analyzed and compared in many different ways. In (Halmetschlager-Funek et al., 2019) several parameters of ten depth cameras were experimentally analyzed and compared. In addition to that, an analysis of the cameras' response to different materials, noise characteristics, and precision were also evaluated. A comparative study on structured light and time-of-flight based Kinect cameras is done in (Sarbolandi et al., 2015). In (Chiu et al., 2019) depth cameras were compared considering medical applications and their specific requirements. Another comparison for medical applications is performed in (Siena et al.,

[a] https://orcid.org/0000-0001-7081-5641
[b] https://orcid.org/0000-0002-9544-424X

2018). A comparison for agricultural applications is performed in (Vit et al., 2018). Analysis for robotic applications is performed in (Jing et al., 2017). In (Anxionnat et al., 2018) several RGB-D sensors are analyzed and compared based on controlled displacements, with precision and accuracy evaluations.

3 METHODOLOGY

3.1 Materials

As aforementioned, the sensors used in this evaluation employ different depth estimation principles, which yields information about the sensor's performance and how these technologies compare to each other (for the specific criteria used).

The SR305 uses coded light, the D415 uses stereo vision, and the L515 uses LIDAR. The camera specifications are represented on table 1. The three cameras were mounted on the standard tripod.

To ensure constant illumination conditions, a LED ring (eff, 2020) was used as the only room illumination source.

Table 1: Sensors resolution (px*px) and range (m).

Sensor	SR305	D415	L515
Depth	640x480	1280x720	1024x768
Color	1920x1080	1920x1080	1920x1080
Range	[0.2 1.5]	[0.3 10]	[0.25 9]

Note that the values on table 1 are upper bounds, meaning that the specifications may vary for different sensors' configurations. It is also important to mention that the D415 range may vary with the light conditions.

3.2 Experimental Setup

Each camera was mounted on a tripod and placed at a distance d of a wall. The wall is white and covers all the field of view of the cameras. The optical axes of the sensors are approximately perpendicular to the wall. Placed above the camera is the light source, above described. The light source points to the wall in the same direction as the camera. For practical reasons, the light source is slightly behind the camera so that the camera does not interfere with the light. A laptop is placed behind the camera where the camera software is executed and where the images are stored. All the experiments took place at night, avoiding any unwanted daylight. Hence, the room's light was kept constant between experiments and always sourced by the same element.

The camera, light source, and laptop were placed on top of a structure. We wanted everything to be high relative to the ground to ensure that the sensors captured neither floor nor ceiling. For each distance at which the cameras were placed, 100 images were acquired. The distances for which both D415 and L515 were tested are 0.5m, 0.75m, 1m, 1.25m, 1.5m, 1.75m, 2m, 2.5m, 3m, and 3.5m. The furthest distance was the maximum distance for which neither floor nor ceiling appeared on the images. The SR305 was tested at 0.3m, 0.4m, 0.5m, 0.75m, 1m, 1.25m, and 1.5m. In this case, the furthest distance is the maximum specified range for the SR305 sensor.

The experiments started at the closest distance. The sensors were switched right after the other sequentially. After all the images were obtained at that distance, all the structure was moved away from the wall by the aforementioned intervals. The structure moved approximately perpendicularly to the wall.

For the D415 and the L515 sensors, we used custom configurations. For the SR305 we used the default configuration. These configurations were the same as those of table 1.

3.3 Software

To deal with the sensors, the Intel RealSense SDK 2.0 was used. The Intel RealSense Viewer application was used to check the sensors' behavior right before each execution, to check for the direction of the optical axis and distance. All the other tasks were executed using custom code and the librealsense2 library. These tasks include both image acquisition and storing, camera configuration, and point cloud generation. This part of the work was executed using Ubuntu. All the statistical evaluation was performed in MatLab, on Windows 10.

3.4 Experimental Evaluation

3.4.1 Performance

The performance of the sensors was measured in two ways. First, we calculated the average number of points for which the sensor failed to measure depth and the standard deviation of the same number of points. Then we do the same for outliers.

Whenever the Intel RealSense SDK 2.0 and camera fail to measure the depth at some point, the corresponding depth is defined as zero. Hence, all we do here is to count pixels in the depth image with a depth equal to zero.

Depth values also contain outliers. Outliers can be defined in several ways. In this case, we considered

as an outlier every point with a depth value differing 10cm from the expected distance, given the specific geometric configuration and setup.

As described in the Intel RealSense D415 product DataSheet (D41, 2020), the D415 sensor has an invalid depth band, which is a region in the depth image for which depth cannot be computed.

The coordinate system of the left camera is used as the reference coordinate system for the stereo camera. The left and right cameras have the same field of view. However, due to their relative displacement, there is an area in the left image for which it is impossible to compute disparities since the corresponding 3D volume is not visible in the right camera. It results in a non-overlap region of the left and right cameras for which it is impossible to measure depth. This region appears in the image's leftmost area and is illustrated in figure 1. The total number of pixels in the invalid depth band can be calculated in pixels as follows:

$$InvalidDepthBand = \frac{VRES * HRES * B}{2 * Z * tan(\frac{HFOV}{2})} \quad (1)$$

Where $VRES$ and $HRES$ stand for vertical and horizontal resolution respectively (720px and 1280px), B is the baseline $\rightarrow$ 55mm, Z is the distance of scene from the depth module $\rightarrow d$ and $HFOV$ is the horizontal field of view $\rightarrow 64°$.

Bearing that in mind, the pixels in the invalid depth band were ignored in our calculations.
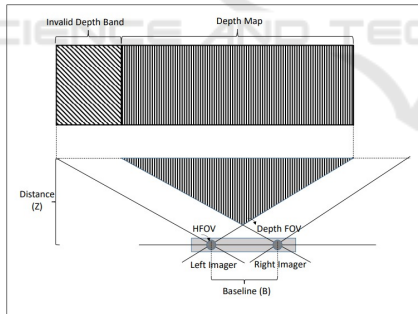
Figure 1: Invalid Depth Band.

3.4.2 Plane Fitting

Point clouds were first obtained using the depth data, the image pixel coordinates, and the camera intrinsics. This is possible because we have depth information, letting the coordinate z be equal to the measured depth at that point, i.e., $z = d_m$ the following equations can be applied:

$$x = z * \frac{u - pp_x}{f_x} \quad (2) \qquad y = z * \frac{v - pp_y}{f_y} \quad (3)$$

Where (u, v) are the pixel coordinates, (pp_x, pp_y) are the coordinates of the principal point, f_x and f_y

are the focal lengths in pixel units.

The point clouds correspond to a wall. Thus it is possible to fit a plane to the data.

Since we handle ourselves the outliers, we performed the plane equation's estimation using standard least-squares regression, employing the singular value decomposition, instead of robust approaches such as RANSAC.

The model we want to be regressed to the point clouds is the general form of the plane equation:

$$x * n_x + y * n_y + z * n_z - d = 0 \quad (4)$$

Where $(n_x, n_y.n_z)$ stands for the unit normal, and d stands for distance from the plane to the origin.

If we now build a $n * 4$ matrix from the point clouds with n points, which we will denote as matrix P. We can rewrite equation 4:

$$0 = \underbrace{\begin{bmatrix} x_1 & y_1 & z_1 & -1 \\ x_2 & y_2 & z_2 & -1 \\ \vdots & \vdots & \vdots & \vdots \\ x_n & y_n & z_n & -1 \end{bmatrix}}_{P} \begin{bmatrix} n_x \\ n_y \\ n_z \\ d \end{bmatrix} \quad (5)$$

By computing the singular value decomposition on matrix P as:

$$P = U * \Sigma * V' \quad (6)$$

We can now use the values of the column of matrix V that corresponds to the smallest eigenvalue in matrix Σ, as the parameters n_x^*, n_y^*, n_z^* and d^* of the plane that fit that point cloud. Then, we normalize the plane's normal vector, which will become handy in further calculations and recover the true distance in meters of the plane from the sensor.

3.4.3 Accuracy

For the accuracy analysis, we compute the point-to-plane distance. For each point of the point cloud, we use the fitted plane equation to compute the errors, i.e., the point-to-plane distance. We then calculate the average root mean square error for each set of 100 images as an accuracy measurement. For the sake of comparison, we perform this computation for two different threshold values for outlier rejection ($\pm 10cm$ and $\pm 35cm$), another one where we use all points with the measured depth.

3.4.4 Precision

In this work, precision is measured as per image plane consistency, i.e., how the plane model changes in between images of the same sensor at the same distance. As neither the scene nor the sensor change while taking the pictures, we could expect the models to be the exact same if we had an ideal sensor. Thus, by

measuring the standard deviation of the plane model parameters in between images, we might be able to better understand how consistent the sensors are with their measurements and how this consistency varies with the distance.

Additionally, we also transform the plane's normal vector into spherical coordinates, where we can perform analysis of directional statistics as all the normals are distributed on a spherical surface. Specifically, the circular mean and standard deviation of angles θ and ϕ, and the spherical variance of the normal vectors. Since $\vec{n}_i$ is unitary, its norm ρ is 1.

Let θ and ϕ be the azimuth and altitude angles of $\vec{n}_i$:

$$\theta_i = \arctan \frac{n_{y_i}}{n_{x_i}} \quad (7) \qquad \phi_i = \arctan \frac{n_{z_i}}{\sqrt{n_{x_i}^2 + n_{y_i}^2}} \quad (8)$$

As in (Kanti V. Mardia, 1999), the circular mean of the angles above can be computed as follows:

$$\overline{\theta} = \arctan \frac{\sum\limits_{i=1}^{n} \sin \theta_i}{\sum\limits_{i=1}^{n} \cos \theta_i} \quad (9)$$

$$\overline{\phi} = \arctan \frac{\sum\limits_{i=1}^{n} \sin \phi_i}{\sum\limits_{i=1}^{n} \cos \phi_i} \quad (10)$$

Now, to show how the spherical variance is computed, we need to introduce vector $\overline{\vec{n}}$, which is the vector whose components are the mean of each component of $\vec{n}$. If we now compute the norm of $\overline{\vec{n}}$ and call it $\overline{R}$, the spherical variance is calculated as follows:

$$V = 1 - \overline{R} \quad (11)$$

4 RESULTS

4.1 Performance Analysis

In tables 2, 3 (In Appendix) and figure 2, we show the results for the average number of failed points and the standard deviation of the number of failed points per image (points where the sensor could not compute depth). As it can be verified, the L515 sensor outperforms both D415 and SR305. This sensor not only showed to be capable of estimating more depth data relative to its resolution, but the results also show that that number (of failed points) remains almost constant up until 2 meters of distance. This can be explained by the fact that this sensor uses LIDAR

technology, which is more robust than the stereo vision and coded light approaches since LIDAR directly computes depth.

On the other hand, the D415 sensor shows much better results than the SR305.

A relevant detail of this performance measurement is that the standard deviation of the number of failed depth points for the D415 is not strongly dependent with the distance, whereas that does not seem to be the case for the L515.

Tables 4, 5 (In Appendix) and figure 3 include the results for the number of outliers. Just as it happened in terms of the average number of failed depth points, the data for the D415 camera show an increase in the average number of outliers as the distance increases. On the other hand, the number of outliers for the SR305 seems to decrease with increasing distances. These results are quite different from those presented in table 2 (In Appendix). The main reason for these results is probably because the SR305 camera is estimating a relatively small number of depth points at higher distances, therefore decreasing the probability of outlier occurrences.

To better illustrate this, we show in figure 4 a sample image taken with the SR305 sensor at 1.5 meters of distance, where it is notorious the small amount of points for which this sensor is measuring depth (the dark region represents points where the depth was not computed).

On the other hand, for the case of the L515, the number of outliers is essentially independent of the distance. Even though there is some fluctuation in the numbers, the variation is relatively small. Considering the standard deviation of the number of outliers per image obtained with the L515 at 0.75, 1.5, and 1.75 meters, we can see that it is zero, meaning that the total number of outliers per image stayed constant over the 100 images. This led us to determine the pixels where L515 generated outliers. We found out that the miscalculated points always correspond to the same pixels from the image's leftmost column. We believe that this may be happening to an issue with the camera used in the experiments, which requires further investigation.

4.2 Accuracy Analysis

The results of the accuracy study are represented on table 6 (In Appendix) and in figure 5, where we plot the point-to-plane RMSE distances for the three cameras, taking into account only points whose distances from the expected distance are within 10cm.

Again, the sensor that achieves the best results is the L515. It not only has the lowest average root mean
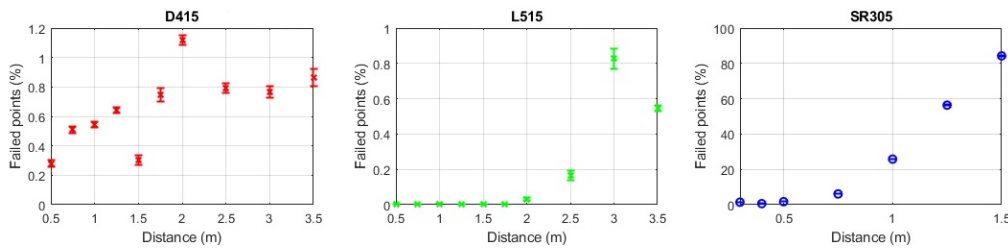
Figure 2: Failed Points - D415 vs L515 vs SR305.
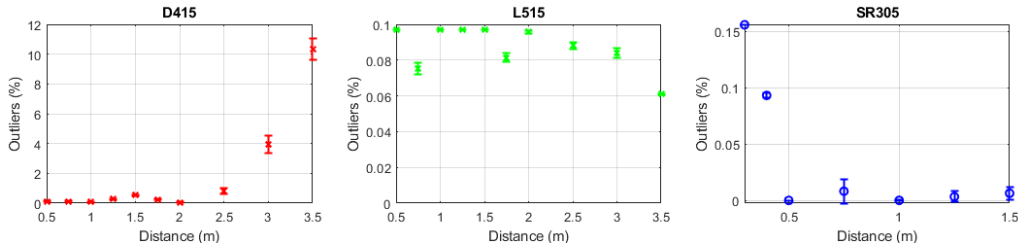
Figure 3: Outliers - D415 vs L515 vs SR305.
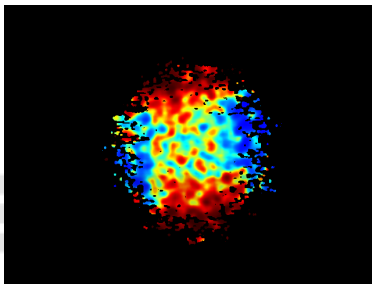
Figure 4: SR305 depth image at 1,5m.

Figure 5: Point-To-Plane RMSE D415 vs L515 vs SR305 - $\pm 10 cm$.

square error per image, but it also shows to be the least sensitive to distance. It should be mentioned that the image acquisition conditions for the L515 were close to being optimal since the images were acquired indoors, without daylight illumination.

In the case of camera D415, its RMSE follows a smooth increasing pattern as it goes further from the wall. On the other hand, the RMSE for the SR305 camera does not vary as smoothly with distance. The RMSE values for this sensor increase until 0.75m and then start to decrease until 1m. In fact, 1 meter is the distance for which the SR305 is optimized (SR3, 2020), therefore one should expect this sensor to work better within this range.

4.3 Precision Analysis

The results show that the camera L515 is significantly more consistent than the other sensors. The results from tables 7 and 8 (In Appendix), show L515 to be more precise in terms of 3D estimation. It is noticeable how this sensor seems to be very consistent between pictures and for different distances.

In table 8 (In Appendix) we show the directional statistics results. The values for the angle θ frequently change in a non-systematic way. This happens because, as ϕ gets closer to $90°$, the components n_x and n_y of the normal vector get closer to zero, which will lead to large variations of the angle θ. For this reason, we omit the azimuth calculations.

The spherical variation behaves just as expected, showing again that the L515 sensor is the most stable and that the measurements from the other two are more distance sensitive.

For ease of comprehension of our precision results, we plot on figures 6 and 7 the standard deviation of parameter d of the plane for all cameras at all distances, and also the spherical variation.
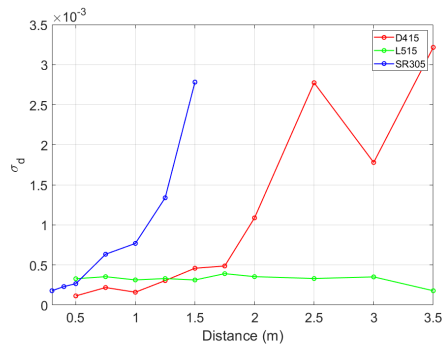
Figure 6: Parameter d standard deviation.
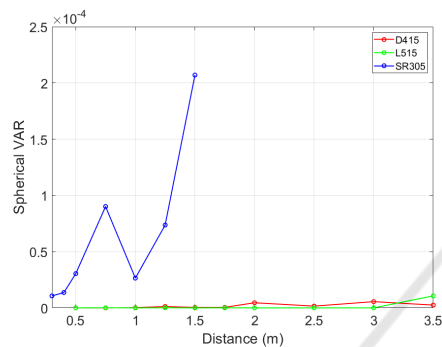
Figure 7: Spherical Variation.

5 CONCLUSION

In this paper, we described a set of experiments performed to compare the depth estimation performance of three RGB-D cameras from Intel, namely the SR305, the D415, and the L515. In general, the results show that the L515 is more accurate and precise than the other two while also providing more stable and consistent measurements in the specific environmental conditions of the experiments (indoors with controlled and stable illumination).

ACKNOWLEDGEMENTS

REFERENCES

(2020). Configurable and powerful ring lights for machine vision. https://www.effilux.com/en/products/ring/effi-ring. (Acessed: 05-10-2020).

(2020). Intel® realsense™ d400 series product family. https://www.intelrealsense.com/depth-camera-d415/. (Acessed: 01-10-2020).

(2020). Intel® realsense™ depth camera sr305. https://www.intelrealsense.com/depth-camera-sr305/. (Acessed: 02-10-2020).

Anxionnat, Adrien, Voros, Sandrine, Troccaz, and Jocelyne (2018). Comparative study of RGB-D sensors based on controlled displacements of a ground-truth model 1. In *2018 15th International Conference on Control, Automation, Robotics and Vision, ICARCV 2018*, pages 125–128.

Cao, Yan-Pei, Kobbelt, Leif, Hu, and Shi-Min (2018). Real-time High-accuracy 3D Reconstruction with Consumer RGB-D Cameras. *ACM Transactions on Graphics*, 1(1).

Chiu, C.-Y., Thelwell, M., Senior, T., Choppin, S., Hart, J., and Wheat, J. (2019). Comparison of depth cameras for three-dimensional reconstruction in medicine. *Journal of Engineering in Medicine*, 233(9).

Fossati, A., Gall, J., Grabner, H., Ren, X., and Konolige, K., editors (2013). *Consumer Depth Cameras for Computer Vision*. Springer.

Halmetschlager-Funek, G., Suchi, M., Kampel, M., and Vincze, M. (2019). An empirical evaluation of ten depth cameras: Bias, precision, lateral noise, different lighting conditions and materials, and multiple sensor setups in indoor environments. *IEEE Robotics and Automation Magazine*, 26(1):67–77.

Jing, C., Potgiete, J., Noble, F., and Wang, R. (2017). A comparison and analysis of rgb-d cameras'depth performance for robotics application. In *Proc. of the Int- Conf. on on Mechatronics and Machine Vision in Practice*.

Kanti V. Mardia, P. E. J. (1999). *Directional Statistics*. Wiley Series in Probability and Statistics. John Wiley & Sons, Inc., Hoboken, NJ, USA, 2nd edition.

P.Rosin, Lai, Y.-K., L.Shao, and Liu, Y., editors (2019). *RGB-D Image Analysis and Processing*. Springer.

Sarbolandi, H., Lefloch, D., and Kolb, A. (2015). Kinect range sensing: Structured-light versus time-of-flight kinect. *Computer Vision and Image Understanding*, 139:1 – 20.

Siena, F. L., Byrom, B., Watts, P., and Breedon, P. (2018). Utilising the Intel RealSense Camera for Measuring Health Outcomes in Clinical Research. *Journal of Medical Systems*, 42(3):1–10.

Vit, Adar, Shani, and Guy (2018). Comparing RGB-D sensors for close range outdoor agricultural phenotyping. *Sensors (Switzerland)*, 18(12):1–17.

Zollhöfer, Michael, Stotko, Patrick, Görlitz, Andreas, Theobalt, Christian, Nießner, M., Klein, R., and Kolb, A. (2018). State of the art on 3D reconstruction with RGB-D cameras. *Computer Graphics Forum*, 37(2):625–652.

APPENDIX

Table 2: Average of failed points ratio per image by distance in meters.

d	D415	L515	d	SR305
0.5	0.2801%	0.0020%	0.3	1.3967%
0.75	0.5099%	0.0001%	0.4	0.6062%
1	0.5414%	0.0023%	0.5	1.6930%
1.25	0.6415%	0.0001%	0.75	6.0734%
1.5	0.3025%	0.0014%	1	25.8181%
1.75	0.7472%	0.0017%	1.25	56.3898%
2	1.1202%	0.0320%	1.5	84.2698%
2.5	0.7945%	0.1648%	—	—
3	0.7660%	0.8263%	—	—
3.5	0.8644%	0.5456%	—	—

Table 3: Standard deviation of failed points ratio per image by distance in meters.

d	D415	L515	d	SR305
0.5	0.0248%	0.0023%	0.3	0.0397%
0.75	0.0224%	0.0003%	0.4	0.0198%
1	0.0195%	0.0050%	0.5	0.0415%
1.25	0.0211%	0.0004%	0.75	0.0783%
1.5	0.0329%	0.0033%	1	0.1282%
1.75	0.0458%	0.0025%	1.25	0.1886%
2	0.0319%	0.0100%	1.5	0.2714%
2.5	0.0335%	0.0278%	—	—
3	0.0378%	0.0570%	—	—
3.5	0.0585%	0.0155%	—	—

Table 4: Average of outliers $\pm 10cm$ ratio per image by distance in meters.

d	D415	L515	d	SR305
0.5	0.1141%	0.0968%	0.3	0.1560%
0.75	0.1112%	0.0753%	0.4	0.0933%
1	0.0667%	0.0968%	0.5	0%
1.25	0.2809%	0.0968%	0.75	0.0081%
1.5	0.5387%	0.0968%	1	3.9062%
1.75	0.2568%	0.0813%	1.25	0.0032%
2	0.0558%	0.0957%	1.5	0.0063%
2.5	0.8361%	0.0882%	—	—
3	3.9436%	0.0839%	—	—
3.5	10.3307%	0.0609%	—	—

Table 5: Standard deviation of outliers $\pm 10cm$ ratio per image by distance in meters.

d	D415	L515	d	SR305
0.5	0.0209%	0%	0.3	0.0004%
0.75	0.0193%	0.0034%	0.4	0.0018%
1	0.0139%	1.2715%	0.5	0%
1.25	0.0226%	0%	0.75	0.0105%
1.5	0.0380%	0%	1	0.0003%
1.75	0.0431%	0.0025%	1.25	0.0046%
2	0.0168%	0.0008%	1.5	0.0057%
2.5	0.1892%	0.0018%	—	—
3	0.5601%	0.0027%	—	—
3.5	0.7226%	0.0001%	—	—

Table 6: Sensors' accuracy in terms of average root mean square point-to-plane distance error per image.

Cam_{dist}	$\pm 10cm$	$\pm 35cm$	All Points
$D415_{0,5m}$	0,002	0,004	0,122
$D415_{0,75m}$	0,003	0,003	0,087
$D415_{1m}$	0,005	0,005	0,079
$D415_{1,25m}$	0,007	0,007	0,037
$D415_{1,5m}$	0,009	0,009	0,139
$D415_{1,75m}$	0,013	0,013	0,293
$D415_{2m}$	0,017	0,017	0,093
$D415_{2,5m}$	0,025	0,027	0,036
$D415_{3m}$	0,036	0,042	0,069
$D415_{3,5m}$	0,045	0,063	0,065
$L515_{0,5m}$	0,001	0,001	134,853
$L515_{0,75m}$	0,001	0,001	202,285
$L515_{1m}$	0,001	0,001	150,913
$L515_{1,25m}$	0,002	0,002	7,556
$L515_{1,5m}$	0,002	0,002	14,588
$L515_{1,75m}$	0,002	0,002	22,389
$L515_{2m}$	0,002	0,002	15,542
$L515_{2,5m}$	0,003	0,003	14,865
$L515_{3m}$	0,004	0,004	25,025
$L515_{3,5m}$	0,006	0,006	13,835
$SR305_{0,3m}$	0,003	0,036	113,994
$SR305_{0,4m}$	0,005	0,005	114,889
$SR305_{0,5m}$	0,008	0,008	0,008
$SR305_{0,75m}$	0,009	0,009	0,009
$SR305_{1m}$	0,005	0,005	0,006
$SR305_{1,25m}$	0,007	0,007	0,008
$SR305_{1,5m}$	0,008	0,008	0,011

Table 7: Camera precision in terms of plane modelling consistency.

Cam_{dist}	$\overline{n_x}$	σ_{n_x}	$\overline{n_y}$	σ_{n_y}	$\overline{n_z}$	σ_{n_z}	$\overline{d}$	σ_d
$D415_{0,5m}$	3,9E-03	2,5E-04	4,1E-03	2,1E-04	1,0E+00	1,5E-06	-5,0E-01	1,1E-04
$D415_{0,75m}$	3,7E-03	3,0E-04	-8,8E-03	2,0E-04	1,0E+00	1,5E-06	-7,5E-01	2,2E-04
$D415_{1m}$	1,7E-02	7,2E-04	-1,3E-03	2,6E-04	1,0E+00	1,3E-05	-1,0E+00	1,6E-04
$D415_{1,25m}$	1,4E-02	1,6E-03	-2,7E-03	3,6E-04	1,0E+00	1,8E-05	-1,3E+00	3,1E-04
$D415_{1,5m}$	1,8E-02	8,7E-04	3,0E-03	4,3E-04	1,0E+00	1,6E-05	-1,5E+00	4,6E-04
$D415_{1,75m}$	2,2E-02	8,5E-04	3,4E-04	5,8E-04	1,0E+00	1,8E-05	-1,8E+00	4,9E-04
$D415_{2m}$	1,3E-02	2,9E-03	2,4E-03	8,6E-04	1,0E+00	2,9E-05	-2,0E+00	1,1E-03
$D415_{2,5m}$	1,0E-02	1,5E-03	-3,2E-03	9,3E-04	1,0E+00	1,4E-05	-2,5E+00	2,8E-03
$D415_{3m}$	1,4E-02	3,2E-03	-5,8E-04	1,1E-03	1,0E+00	3,3E-05	-3,0E+00	1,8E-03
$D415_{3,5m}$	6,6E-03	1,8E-03	1,8E-03	1,3E-03	1,0E+00	1,2E-05	-3,5E+00	3,2E-03
$L515_{0,5m}$	-4,6E-05	6,1E-04	-2,9E-03	2,3E-04	1,0E+00	7,9E-07	-5,0E-01	3,5E-04
$L515_{0,75m}$	1,8E-03	4,6E-04	-2,7E-03	1,6E-04	1,0E+00	7,1E-07	-7,5E-01	3,3E-04
$L515_{1m}$	-1,9E-03	6,1E-04	-5,7E-03	1,5E-04	1,0E+00	1,9E-06	-1,0E+00	3,5E-04
$L515_{1,25m}$	-6,8E-06	3,1E-04	2,1E-03	7,6E-05	1,0E+00	1,9E-07	-1,3E+00	3,1E-04
$L515_{1,5m}$	-3,1E-03	5,2E-04	-9,2E-04	1,9E-04	1,0E+00	1,7E-06	-1,5E+00	3,3E-04
$L515_{1,75m}$	1,8E-03	3,3E-04	3,1E-04	1,0E-04	1,0E+00	6,2E-07	-1,8E+00	3,1E-04
$L515_{2m}$	-8,0E-04	4,5E-04	-5,1E-04	1,7E-04	1,0E+00	4,4E-07	-2,0E+00	3,9E-04
$L515_{2,5m}$	3,2E-04	3,5E-04	-8,7E-04	1,4E-04	1,0E+00	1,7E-07	-2,5E+00	3,5E-04
$L515_{3m}$	-2,1E-03	3,3E-04	-3,9E-03	1,5E-04	1,0E+00	1,1E-06	-3,0E+00	3,3E-04
$L515_{3,5m}$	1,7E-03	4,0E-04	-6,8E-03	8,3E-05	1,0E+00	7,7E-07	-3,5E+00	3,5E-04
$SR305_{0,3m}$	4,4E-03	4,6E-03	-5,6E-03	1,0E-04	1,0E+00	2,7E-05	-3,0E-01	1,8E-04
$SR305_{0,4m}$	7,7E-03	5,2E-03	-8,2E-04	8,7E-05	1,0E+00	6,2E-05	-4,0E-01	2,3E-04
$SR305_{0,5m}$	1,7E-02	7,8E-03	5,2E-03	1,2E-04	1,0E+00	1,6E-04	-5,0E-01	2,7E-04
$SR305_{0,75m}$	-1,7E-02	1,3E-02	-1,3E-04	2,8E-04	1,0E+00	2,6E-04	-7,5E-01	6,3E-04
$SR305_{1m}$	-1,7E-02	7,3E-03	6,6E-03	1,8E-04	1,0E+00	1,0E-04	-1,0E+00	7,7E-04
$SR305_{1,25m}$	-2,7E-02	1,2E-02	-2,3E-03	5,0E-04	1,0E+00	2,6E-04	-1,3E+00	1,3E-03
$SR305_{1,5m}$	-2,3E-02	2,0E-02	-2,9E-03	1,1E-03	1,0E+00	5,8E-04	-1,5E+00	2,8E-03

Table 8: Camera precision in terms of plane normal vector angles standard deviation and spherical variance.

Cam_{dist}	$\overline{\phi}$	σ_ϕ	V	Cam_{dist}	$\overline{\phi}$	σ_ϕ	V
$D415_{0,5m}$	9,0E+01	1,5E-02	5,3E-08	$L515_{1,5m}$	9,0E+01	3,1E-02	1,5E-07
$D415_{0,75m}$	8,9E+01	9,2E-03	6,5E-08	$L515_{1,75m}$	9,0E+01	1,9E-02	5,9E-08
$D415_{1m}$	8,9E+01	4,1E-02	2,9E-07	$L515_{2m}$	9,0E+01	2,4E-02	1,2E-07
$D415_{1,25m}$	8,9E+01	8,5E-02	1,3E-06	$L515_{2,5m}$	9,0E+01	8,6E-03	7,3E-08
$D415_{1,5m}$	8,9E+01	4,9E-02	4,7E-07	$L515_{3m}$	9,0E+01	1,4E-02	6,5E-08
$D415_{1,75m}$	8,9E+01	4,9E-02	5,3E-07	$L515_{3,5m}$	9,0E+01	6,2E-03	8,3E-08
$D415_{2m}$	8,9E+01	1,6E-01	4,6E-06	$SR305_{0,3m}$	9,0E+01	1,5E-01	1,1E-05
$D415_{2,5m}$	8,9E+01	7,9E-02	1,6E-06	$SR305_{0,4m}$	9,0E+01	3,0E-01	1,4E-05
$D415_{3m}$	8,9E+01	1,7E-01	5,6E-06	$SR305_{0,5m}$	8,9E+01	4,2E-01	3,1E-05
$D415_{3,5m}$	9,0E+01	1,0E-01	2,5E-06	$SR305_{0,75m}$	8,9E+01	7,0E-01	9,0E-05
$L515_{0,5m}$	9,0E+01	1,4E-02	2,1E-07	$SR305_{1m}$	8,9E+01	3,2E-01	2,7E-05
$L515_{0,75m}$	9,0E+01	1,2E-02	1,2E-07	$SR305_{1,25m}$	8,8E+01	5,6E-01	7,4E-05
$L515_{1m}$	9,0E+01	1,8E-02	2,0E-07	$SR305_{1,5m}$	8,9E+01	1,0E+00	2,1E-04
$L515_{1,25m}$	9,0E+01	4,8E-03	5,2E-08	—	—	—	—